Editors' Suggestion

Single-spin spectroscopy of spontaneous and phase-locked spin-torque-oscillator dynamics

Adrian Solyom,[1] Michael Caouette-Mansour,[1] Brandon Ruffolo,[1] Patrick Braganca,[2] Lilian Childress,[1] and Jack C. Sankey[1,*]

[1] *Department of Physics, McGill University, 3600 Rue University, Montreal, Quebec H3A 2T8, Canada*
[2] *Western Digital, San Jose, California 95119, USA*

(Received 29 July 2023; revised 4 October 2023; accepted 11 October 2023; published 28 November 2023)

We employ nitrogen-vacancy (N-*V*) magnetometry to measure the stray field dynamics of a ferromagnetic permalloy nanowire driven by spin-orbit torques. Specifically, we observe the optically detected magnetic resonance (ODMR) signatures of both spontaneous dc-driven magnetic oscillations and phase locking to a second harmonic drive, developing a simple macrospin model that captures the salient features. We also observe signatures of dynamics beyond the macrospin model, including an additional ODMR feature (associated with a second spin-wave mode) and one mode sapping power from another. Our results provide additional insight into N-*V*-spin-wave coupling mechanisms, and represent a new modality for subwavelength N-*V* scanned probe microscopy of nanoscale magnetic oscillators.

DOI: 10.1103/PhysRevApplied.20.054055

I. INTRODUCTION

When compared to architectures employing field-effect transistors, logical devices using spin degrees of freedom to store and carry information show promise for energy-efficient processing [1–4]. Moreover, the nonlinear nature of such magnetic devices offers potential new avenues for massively parallel neuromorphic computing [5–11]. The development of this new technology requires characterization methods appropriate for a range of devices, such as logic gates [4] and oscillator arrays [12]. Established techniques such as magnetoresistive readout [13–19], Brillouin light scattering [20–22], x-ray scattering [23,24], and time-resolved magneto-optic Kerr effect measurements [1,25,26] allow for excited magnetic spin waves (SWs) to be detected and measured in frequency space, but each method naturally causes backaction on the device and/or is limited in spatial resolution. To address these two issues, solid-state spins have been developed as atomic scale, minimally invasive probes of the stray fields surrounding SW excitations. Among spin-based magnetometers, the nitrogen-vacancy (N-*V*) defect in diamond is currently the most studied, and can be placed within nanometers of the sample, enabling scanned probe readout of SWs with small wavelengths. To date, N-*V* centers have been used to probe ferromagnetic phenomena, including vortex cores [27–29], domain walls [30], oscillators [31], magnetic tunnel junctions [32], SW dispersion [33,34], and SW scattering [35].

In this study, we employ N-*V* magnetometry to measure the stray field of a metallic ferromagnetic nanowire driven by dc and microwave spin-orbit torques (plus associated magnetic fields) generated by current in a platinum capping layer. Following Refs. [34,36,37], we parametrically drive SW modes at twice their natural frequency, directly observing the response in the N-*V* center's optically detected magnetic resonance (ODMR) spectrum at the SW frequency (without directly driving the N-*V* transitions). To extend previous work, we design the present device with dimensions small enough to suppress Suhl instabilities [38,39], allowing it to act as a spin-torque oscillator (STO) with large-amplitude SW oscillations driven by dc bias alone. Below the STO threshold current, we observe parametrically driven large-angle precession in the ODMR spectrum, and resolve two SW modes, one of which produces a signature of auto-oscillation above the threshold current. In this regime, the ODMR spectrum also exhibits evidence of coupling between the modes, as parametrically driving the second saps power from the first. Furthermore, we identify the ODMR spectral signature of phase locking between auto-oscillations and a second-harmonic drive by comparing our ODMR spectra with a simple model coupling a macrospin [36] to an N-*V*, and find semiquantitative agreement with the behavior of the fundamental SW mode. Finally, we perform spin relaxometry with the N-*V* to observe the magnetic noise from the SW modes as the bias is increased above the STO threshold. The results from this simple testbed system demonstrate the potential utility of N-*V* magnetometry in STO characterization that should be especially

*jack.sankey@mcgill.ca

useful when applied in a scanned-probe measurement [34,40–43].

II. DEVICE FABRICATION AND TRANSPORT CHARACTERIZATION

We study Py($Ni_{80}Fe_{20}$, 5 nm)/Pt(5 nm) nanowires with nominal lateral dimensions 3×0.3 μm^2 fabricated on an electronic grade diamond substrate (see Appendix A for fabrication details). Figure 1(a) shows an optical micrograph of the device after the electrical leads have been deposited with a 300-nm overlap on either side of the nanowire. The dashed area in Fig. 1(b) is a confocal fluorescence image taken (by focusing green 532-nm light to a scanned point and collecting red fluorescence with the same objective) before depositing the leads. Individual N-V centers appear as bright spots. The device, which blocks light from entering or leaving the diamond substrate, appears as a shadow highlighted with a white rectangle, and the N-V used to probe the stray field is located within the dotted white circle. Throughout this study, a magnetic field is applied along an axis nearly parallel to the diamond's [111] direction—orthogonal to the current flow in the nanowire and (nearly) parallel to the N-V symmetry axis (canted approximately 35° out of plane)—such that the total "external" field B_{ext}, including that of the static stray field of the proximal nanowire (but not the Oersted field from currents passing through the device), is well aligned with the N-V axis over the range of fields studied [36].

We electrically characterize the magnetic modes by performing spin-transfer ferromagnetic resonance (ST-FMR), using a pulse-modulated lock-in technique [36]. The measurement works by detecting the average voltage V_{MR} resulting from the mix-down between an applied microwave (MW) current and magnetoresistance (MR) oscillations associated with magnetic precession (averaged over the volume of the magnetic layer). Figure 1(c) shows such measurements performed on the device while sweeping the drive frequency ν_{MW} and applying a magnetic field of $B_{ext} = 41$ mT with current $I(t) = I_{MW}\cos(2\pi\nu_{MW}t) + I_{bias}$ comprising microwave drive amplitude $I_{MW} = 1$ mA and a dc bias I_{bias}. At zero bias (top blue curve, scaled by factor of 5 for clarity), we observe a characteristic Fano line shape at 4 GHz, as expected for ferromagnetic resonance driven by a combination of spin Hall torque and field generated by the current [36]. The small signal is due to the minimal drive and readout efficiency occurring when the magnetization is oriented mostly along the in-plane hard axis. (The omnipresent features in the gray regions are artifacts arising from antenna modes of the waveguides and wirebond, and should be ignored.)

With increased dc bias, spin-orbit torques (SOTs) from the platinum layer effectively antidamp the Py layer's magnetic motion, permitting excitation of large-amplitude, narrow-linewidth SW oscillation, and parametrically driven oscillations near twice the fundamental frequency (8 GHz) [36]. In this regime, evidence of two spin-wave modes (SW1 and SW2) can be resolved. The lowest-frequency peak has the largest (spatially averaged) MR response, consistent with quasiuniform precession, while the second, smaller peak is likely one of the next higher-order modes (i.e., with one or two nodes splitting the long axis). A second (subtle) change in lineshape near and above 4.47 mA *might* suggest the onset of dc-driven auto-oscillations phase locked to the drive (similar to the changes observed in Ref. [17]).

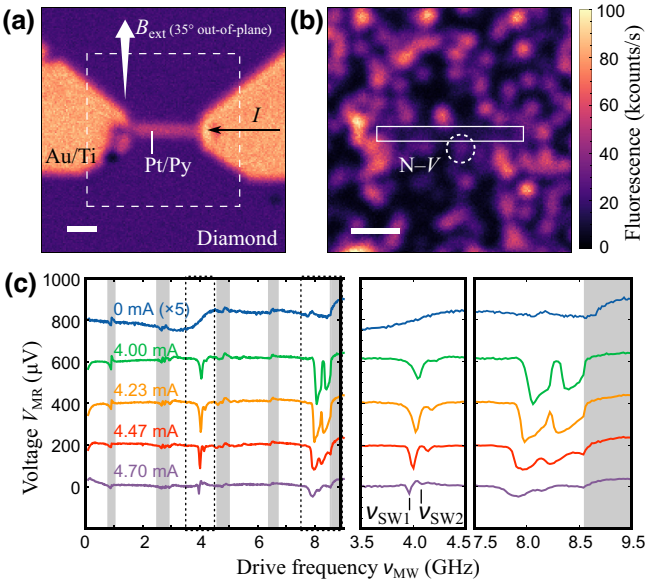

FIG. 1. Device geometry and transport measurements. (a) Reflected confocal image of the device with overlapping leads attached. The dashed box indicated the region imaged in (b). (b) Fluorescence confocal image of N-V centers near the device, taken prior to the deposition of electrical leads in (a). The white rectangle indicates the location of the device (a shadow in fluorescence), while the dotted circle highlights the location of the N-V center used for measurements in this study. Scale bars in (a) and (b) are 1 μm each. (c) ST-FMR measurements performed with $B_{ext} = 41$ mT, $I_{MW} = 1$ mA, and with varied I_{bias}. The gray shaded regions indicate "untrustworthy" frequency ranges with low transmission to the device, while dashed boxes define the enlarged panels on the right. The narrow phase-locked response of the first (second) SW modes are marked ν_{SW1} (ν_{SW2}), while the same modes are excited parametrically at twice their resonant frequencies in the right-most panel. Data are offset vertically for clarity, and the zero-bias trace is scaled by a factor of 5 to enhance visibility.

III. ODMR MEASUREMENTS

In contrast to the electrical measurements above, the onset of auto-oscillation and phase locking presents a

qualitatively distinctive feature in the ODMR spectrum of a single proximal N-V spin. In this detection modality, the N-V is continuously excited with green 532-nm laser light focused through a 0.95-NA air objective, while the resulting fluorescent emission (filtered by a 635-nm long pass) is collected by the same lens and monitored by a single-photon counter. The optical excitation polarizes the N-V into the $m_s = 0$ spin state, which fluoresces more brightly than the ± 1 states. Then, any oscillating magnetic fields (coherent or noisy) at frequencies near the spin resonance can drive the N-V into a spin mixture with reduced fluorescence.

Figures 2(a)–2(c) show fluorescence data obtained by continuously applying a microwave current $I_{MW} = 0.5$ mA through the wire while sweeping the applied field B_{ext} and microwave frequency ν_{MW}. Columns (i)–(iv) are the same data taken at varied I_{bias} to show the transition through the SW's critical current of about 4.4 mA. The frequency ranges in Figs. 2(b) and 2(c) show the "standard" ODMR response from driving the N-V spin transition at frequencies of $\nu_{\pm}$ (the splitting of which increases with field due to the Zeeman effect) directly with the field from I_{MW}. Each vertical slice is simultaneously fit to two Lorentzian dips of the same width and depth to extract the frequencies $\nu_{\pm}$, as well as the magnitude of the (mixed-spin) fluorescence that occurs on resonance, which is subsequently used to normalize all vertical slices in Fig. 2 (this normalization compensates for slow drifts in laser power and alignment during data acquisition), including the data near the second harmonics in row (a). Note that the gradual reduction in fluorescence at higher B_{ext} arises from optically induced spin mixing associated with fields orthogonal to the N-V near the excited-state level anticrossing [44]. Spin-wave frequencies ν_{SW1} (ν_{SW2}) obtained by ST-FMR are superimposed as open circle (square) symbols and connected with guide lines in Fig. 2(b), while the second harmonics of these same frequencies are plotted in Fig. 2(a). The solid lines show $\nu_{\pm}$ and their harmonics for reference. In contrast to the magnetoresistive readout above, here we have reduced I_{MW} to 0.5 mA so that it is insufficient to parametrically drive the SW modes with 4 mA of bias [Fig. 2(a)(i)].

Operating near the second harmonic offers an attractive method of probing for magnetic signatures, as the N-V is insensitive to the direct drive from I_{MW}, while maintaining sensitivity to the SW stray fields near $\nu_{SW1,2}$. For example, as I_{bias} approaches the STO threshold (ii), the expected feature appears in (a) at $B_{ext} = 40$ mT where the parametrically driven SW1 and N-V frequencies are in resonance [36]. As the bias is increased beyond the STO threshold (iii), several new features emerge. First, SW auto-oscillations directly drive the N-V spin at 41 mT (where $\nu_{SW1} \approx \nu_{+}$); this free-running STO signal is independent of the drive I_{MW} whenever ν_{MW} is far from $2\nu_{SW1}$, leading to a vertical stripe of reduced fluorescence. Closer to $2\nu_{SW1}$, the stripe bends, with "tails" that extend well beyond the resonance condition. As discussed below, these features are reasonably captured by a simple macrospin model, but we can also anticipate the behavior qualitatively. At field strengths where $\nu_{SW1} = \nu_{+}$, i.e., when the drive frequency ν_{MW} approaches twice the STO resonance frequency, the magnetic oscillations can phase lock with the drive, pulling their frequency out of resonance with ν_{+} and returning the fluorescence to the higher $m_s = 0$ value, e.g., near 8 GHz at 41 mT. When the phase-locked SW mode is driven to resonance with $\nu_{MW} = 2\nu_{+}$ again, it drives N-V transitions, and the fluorescence returns to the lower mixed-state value. Additionally, at fields away from 41 mT (and where $\nu_{SW1} \neq \nu_{+}$), the unlocked STO and MW drive "beat" in and out of phase with each other at the difference frequency

$$\Delta\nu_{drive} = \nu_{MW} - 2\nu_{SW1} \tag{1}$$

such that the drive *modulates* the STO amplitude (and frequency). This generates sidebands at $\nu_{SW1} \pm \Delta\nu_{drive}/2$ that can drive N-V transitions, producing lower fluorescence "tails" extending away from the locked region. These are most easily seen in Fig. 2(d), which shows the same data as in (a), but transformed onto axes of N-V "probe" detuning

$$\Delta\nu_{probe} = \nu_{+} - \nu_{SW1} \tag{2}$$

and "drive" detuning $\Delta\nu_{drive}$, with an added dotted line along $\Delta\nu_{drive} = \Delta\nu_{probe}$ for reference. As expected for a second-harmonic drive, the parametrically driven and phase-locked dips in (ii) and (iii) occur at probe detunings of $\Delta\nu_{probe} = \Delta\nu_{drive}/2$ [45]. Above the STO threshold [(iii) and (iv)], we also see auto-oscillations as a horizontal line at $\Delta\nu_{probe} = 0$, while the tails asymptote toward unity slope, consistent with I_{MW} adding modulation sidebands to the SW oscillation. Between the phase-locked and asymptotic regimes, the ODMR feature transitions continuously, indicating that the drive may be pulling the oscillator frequency without fully phase locking. We note that this spectral feature is suppressed in (iii) near the first harmonic [in (b)], as expected by symmetry for our geometry; the spin-orbit torques are nearly aligned with the average magnetization of the SW oscillations, and so directly driving its precession is inefficient.

In Fig. 2(a)(iii), we also observe a second dip at $B_{ext} = 36$ mT near the resonance condition $\nu_{SW2} = \nu_{+}$ for SW2. As such, we associate this feature with parametric driving of SW2. Interestingly, when the N-V is resonant with the auto-oscillations of SW1 (41 mT), we observe a brightening of the fluorescence [arrows in (a)(iii) and (d)(iii)] while driving near $2\nu_{SW2}$, suggesting that our parametric drive of SW2 has quenched the auto-oscillations of SW1. Note that this tendency for one SW mode to dominate the spectrum has been a ubiquitous feature since the first observation of

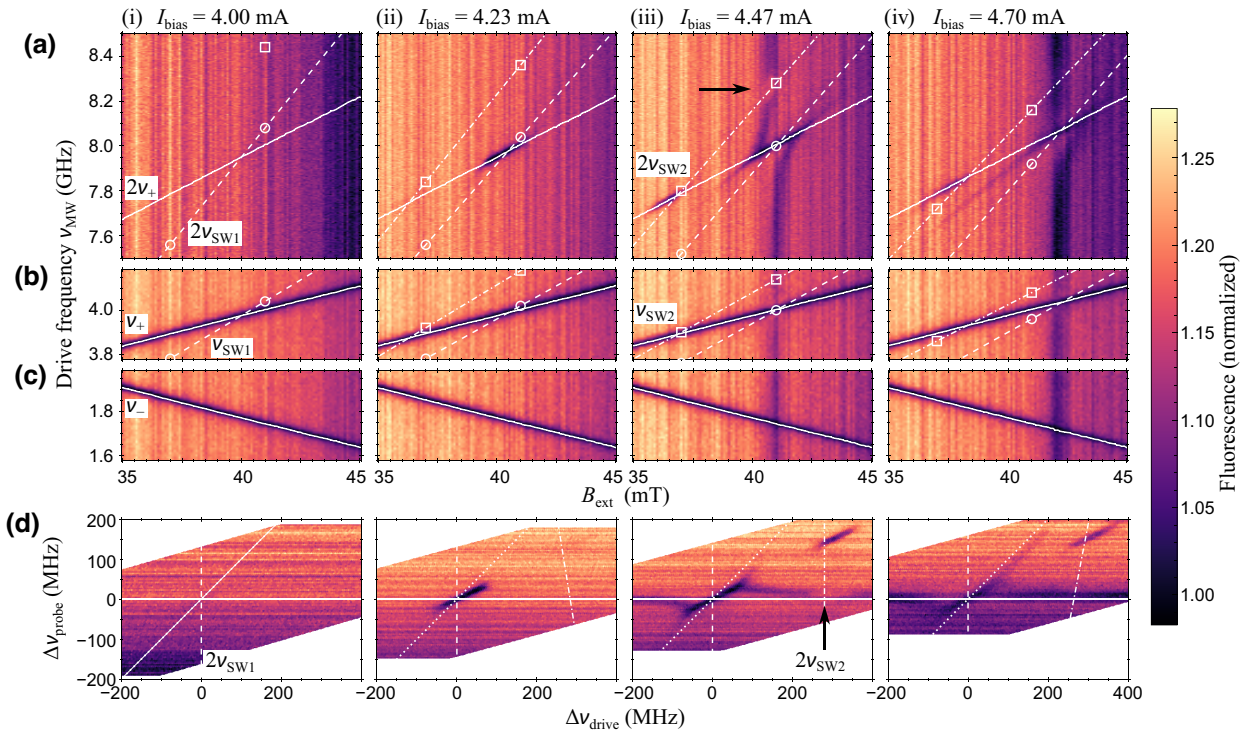

FIG. 2. ODMR measurements. (a)–(c) ODMR measurements of the probe N-V center near the STO resonance. Circles (squares) represent the ν_{SW1} (ν_{SW2}) mode frequency measured in transport [as shown in Fig. 1(c)], while the dash-dot (dashed) lines are guides to the eye connecting the measurements. Solid white lines are the frequencies fit to the ν_+ and ν_- N-V transitions in rows (b) and (c), and represent $2\nu_+$ in row (a). Each vertical slice of data is normalized by the mixed-state fluorescence of the $\nu_\pm$ transitions. (d) Same data as in (a), but transformed into axes of probe versus drive detunings from the SW1 mode. The dotted diagonal line shows where $\Delta\nu_{probe} = \Delta\nu_{drive}$. Columns (i)–(iv) show the evolution of the measurement as the bias is swept from 4.0 to 4.7 mA. The black arrows in (a)(iii) and (d)(iii) show evidence of power sapping from the STO when parametrically driving SW2.

an STO [13]. For dc-driven systems, there exist regimes of "mode hopping" to (and from) other dynamical states [46], but we do not see evidence of this here, likely due to the limited range of explored bias.

Finally, as the bias is further increased [(iv)], we see the SW features darken and broaden, with the modulation tail visible over a greater range of fields. Additionally, the brightening associated with driving SW2 parametrically while probing SW1 is suppressed, suggesting that SW1 is no longer fully quenched.

IV. MACROSPIN MODELING

The signatures of parametric drive, auto-oscillation, and phase locking are reasonably captured by a simple model coupling macrospin (uniform) magnetization dynamics to an N-V probe via the stray field. Specifically, the magnetization's unit vector $\mathbf{m}$ follows the Landau-Lifshitz equation

$$\frac{d\mathbf{m}}{dt} = -\frac{\gamma}{\mu_0}\mathbf{m}\times\mathbf{B}_{\text{eff}} - \frac{\alpha}{\mu_0}\mathbf{m}\times(\mathbf{m}\times\mathbf{B}_{\text{eff}}) + \mathbf{q}_{\text{SOT}} \quad (3)$$

with gyromagnetic ratio $\gamma = 28$ GHz/T, vacuum permittivity μ_0, Gilbert damping coefficient $\alpha = 0.04$ (estimated from ST-FMR measurements [36]), plus an added spin-orbit torque [Fig. 3(a)]

$$\mathbf{q}_{\text{SOT}} = \frac{\Theta_{\text{SH}}}{M_s L_y L_z^2}\frac{\mu_0\gamma\hbar}{2e} I_{\text{Pt}}\hat{y} \quad (4)$$

with effective spin Hall angle $\Theta_{\text{SH}} = 0.1$ in the Pt layer (chosen so that the observed and modeled STO threshold currents match), Py saturation magnetization $M_s = 760$ [47], magnetic layer width $L_y = 300$ nm and thickness $L_z = 5$ nm, and Pt current

$$I_{\text{Pt}} = \frac{\rho_{\text{Py}}}{\rho_{\text{Pt}} + \rho_{\text{Py}}} I, \quad (5)$$

where $\rho_{\text{Pt}} = 21.9\ \mu\Omega$ cm and $\rho_{\text{Py}} = 65.2\ \mu\Omega$ cm [48]. The first term in Eq. (3) describes precession about an effective field

$$\mathbf{B}_{\text{eff}} = \mathbf{B}_I + \mathbf{B}_{\text{ext}} + \mathbf{B}_{\text{demag}} + \mathbf{B}_{\text{therm}}, \quad (6)$$

where

$$\mathbf{B}_I = \eta I \hat{y} \tag{7}$$

is the average current-generated field experienced by $\mathbf{m}$ with efficiency $\eta = 1$ T/A (roughly estimated from the geometry and resistivities of the metals, and consistent with the ST-FMR lineshape [36]),

$$\mathbf{B}_{\text{ext}} = B_{\text{ext}}\left(\sqrt{\frac{2}{3}}\hat{y} + \frac{1}{\sqrt{3}}\hat{z}\right) \tag{8}$$

is the externally applied field (magnitude B_{ext}),

$$\mathbf{B}_{\text{demag}} = -\mu_0 M_s \mathbf{N} \cdot \mathbf{m} \tag{9}$$

is the demagnetizing field with (shape-defined) tensor $\mathbf{N}$, approximated here as that of an ellipsoid with only diagonal elements $N_{xx} = 0$, $N_{yy} = L_z/(L_y + L_z)$, and $N_{zz} = L_y/(L_y + L_z)$ [36,49], and $\mathbf{B}_{\text{therm}}$ is a stochastic Langevin field [50] drawn from a Gaussian distribution of standard deviation $\sqrt{4\mu_0\alpha k_B T/\gamma M_s V \Delta t}$ at each time step (of duration Δt) and dimension separately, with Boltzmann constant k_B, temperature $T = 300$ K, and magnetic volume $V = L_x L_y L_z = 4.5 \times 10^{-21}$ m^3 (estimated from the nominal Py dimensions). The second term in Eq. (3) describes the magnetization's descent down the potential energy gradient due to damping α. For each applied field and drive current, we allow the simulation to reach a steady state, then average the power spectral densities over 16 iterations of $T_{\text{sim}} = 20$ μs each.

Once the time-dependent magnetization is computed, the resulting N-V dynamics are modeled from the local field at the position of the N-V, comprising the static applied field $\mathbf{B}_{\text{ext}}$, the Oersted field $\mathbf{B}_{\text{Oe}}$ from the current in both layers of the wire, and the dipolar field $\mathbf{B}_{\text{dip}}$ from the magnetic layer. The Oersted field is computed assuming translational symmetry along $\hat{x}$, while the dipolar field is obtained by assuming uniform magnetization of the Py along $\mathbf{m}$ and integrating over the layer's volume [see Fig. 3(b)]. We use $\mathbf{r}_{\text{NV}} = -(240, 300, 60)$ nm for the position of the N-V probe relative to the center of the device, estimated from the optical measurements in Fig. 1(b) (determines xy) and SRIM calculations to determine the implantation depth [36]. The resulting time-dependent field at the N-V is then used to calculate three relevant quantities: first, the N-V spin transition frequency is set by the time-averaged field

$$\langle B_j \rangle = \frac{1}{T_{\text{sim}}} \int_0^{T_{\text{sim}}} \mathbf{B}_{\text{dip}} \cdot \mathbf{e}_j \, dt, \tag{10}$$

where T_{sim} is the simulation's duration and the $\mathbf{e}_j$ are three orthogonal unit vectors

$$\mathbf{e}_X = \hat{x}, \tag{11}$$

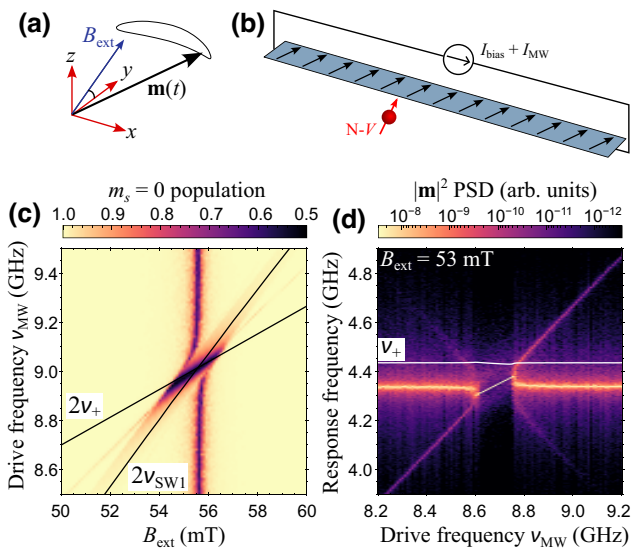

FIG. 3. Simulated ODMR. (a) Axis definitions and typical large-amplitude trajectory of the magnetization $\mathbf{m}(t)$ in the macrospin simulation. (b) The time-varying magnetic field at the N-V probe location—which determines its population and fluorescence—arises from the magnetic layer's integrated dipolar field, the Oersted field from applied currents, and the external applied field. (c) Calculated $m_s = 0$ population when the nanowire is driven with $I_{\text{bias}} = 4.47$ mA and $I_{\text{MW}} = 0.5$ mA, which reproduces the STO "vertical stripe," phase locking region, and modulation sideband tails observed in Fig. 2(a)(iii). (d) Power spectral density (PSD) of the macrospin model under the same conditions as (c), with a fixed magnetic field of $B_{\text{ext}} = 53$ mT, clearly showing the phase-locked region from 8.6–8.75 GHz drive, frequency pulling near this region, and the modulation sidebands outside this region. The white line shows the N-V frequency, which is slightly affected by the changing average magnetization.

$$\mathbf{e}_Y = \frac{1}{\sqrt{3}}(\hat{y} - \sqrt{2}\hat{z}), \tag{12}$$

$$\mathbf{e}_Z = \frac{1}{\sqrt{3}}(\sqrt{2}\hat{y} + \hat{z}), \tag{13}$$

reckoned relative to the N-V symmetry axis $\mathbf{e}_Z$; second, the Rabi frequency

$$\Omega_R = 4\pi\gamma_{NV} \frac{\int_0^{T_{\text{sim}}} \mathbf{B}_{\text{dip}} \cdot \boldsymbol{\sigma}(\nu_{\text{MW}}/2) dt}{\int_0^{T_{\text{sim}}} \boldsymbol{\sigma}(\nu_{\text{MW}}/2) \cdot \boldsymbol{\sigma}(\nu_{\text{MW}}/2) dt} \tag{14}$$

is calculated from coherent, synchronized magnetic oscillations at half the microwave drive frequency ν_{MW}, where $\gamma_{NV} = 28$ GHz/T is the N-V spin's gyromagnetic ratio and $\boldsymbol{\sigma}(\nu) = e^{i2\pi\nu t}\mathbf{e}_X + ie^{i2\pi\nu t}\mathbf{e}_Y$ is the transverse component of

the spin's corotating frame; third, the induced relaxation rate

$$\Gamma_1 = 4\pi\gamma_{NV}^2 T_{\rm sim}\left|\frac{\int_0^{T_{\rm sim}} \mathbf{B}_{\rm dip}\cdot\boldsymbol{\sigma}(\nu_+)dt}{\int_0^{T_{\rm sim}} \boldsymbol{\sigma}(\nu_+)\cdot\boldsymbol{\sigma}(\nu_+)dt}\right|^2 \qquad (15)$$

is found from the transverse field noise spectrum at the transition frequency ν_+. With these parameters, we can estimate the steady-state $m_s = 0$ population using a two-level optical Bloch equation [51] (see Appendix C).

By varying the applied field and drive frequency, we simulate data in Fig. 3(c) over the same parameter range as the measurement in Fig. 2(a)(iii). For the chosen parameters, the simulation provides somewhat quantitative agreement with the key features in the measured ODMR spectrum, though there are some exceptions. First, the macrospin approximation precludes additional SW modes or associated interactions. Second, the simulated resonance between the N-V and the magnet occurs at higher fields than experimentally observed, since the macrospin mode generally has lower frequency than a spatially varying mode that is "stiffened" by the exchange field.

Despite this, our simple toy model validates the above interpretation of the ODMR signatures associated with phase-locking and freely oscillating STO regimes, including frequency pulling near the phase-locking regime, and a strong phase-locked response at $2\nu_+$. We also clearly see the modulation sidebands occurring at the expected frequencies. To make these features more explicit, Fig. 3(d) shows the power spectral density of the simulated macrospin (the summed contributions of $\mathbf{m}$'s x, y, and z components), with the same axes as those of Fig. 2(d), but a color scale associated with $\mathbf{m}$ instead of N-V fluorescence. At $\nu_{\rm MW} = 4.35$ GHz, we observe the expected free-running STO, whose frequency is pulled down as the drive approaches 8.6 GHz, at which point the magnetization locks phase with the drive, following the frequency $\nu_{\rm MW}/2$ until it unlocks at 8.75 GHz drive, where the STO is again free running at a higher-than-unperturbed frequency. Modulation sidebands appear when the response (probe) and drive detunings are equal, as expected. As a caveat, note that this comparison is only rigorously valid outside the phase-locked regime, since, within it, the large Rabi frequency of the magnetization drive broadens the N-V center's ODMR linewidth rather than producing a delta-function frequency response expected from a coherent oscillation.

V. LIFETIME MEASUREMENTS

Finally, we can study STO dynamics in the absence of microwave driving by performing all-optical relaxometry with the N-V probe. Specifically, we perform lifetime measurements using the pulse sequence shown in Fig. 4(a), first initializing the N-V into $m_s = 0$ with a 532-nm laser pulse, then allowing variable "dark" evolution time τ between 5 and 25 μs, and finally reading out the new spin state with another laser pulse. The signal fluorescence is normalized to the counts measured during a later "reference" time to minimize slow drifts in the optical paths. A simplified single-decay model [Fig. 4(b)] is used to extract the relaxation rate Γ_+, assuming that the STO is the dominant source of relaxation during the evolution time and that it only drives relaxation between spin states 0 and +1.

Figures 4(c) and 4(d) show the fluorescence from the relaxation measurements with $\tau = 5$ and 25 μs as the

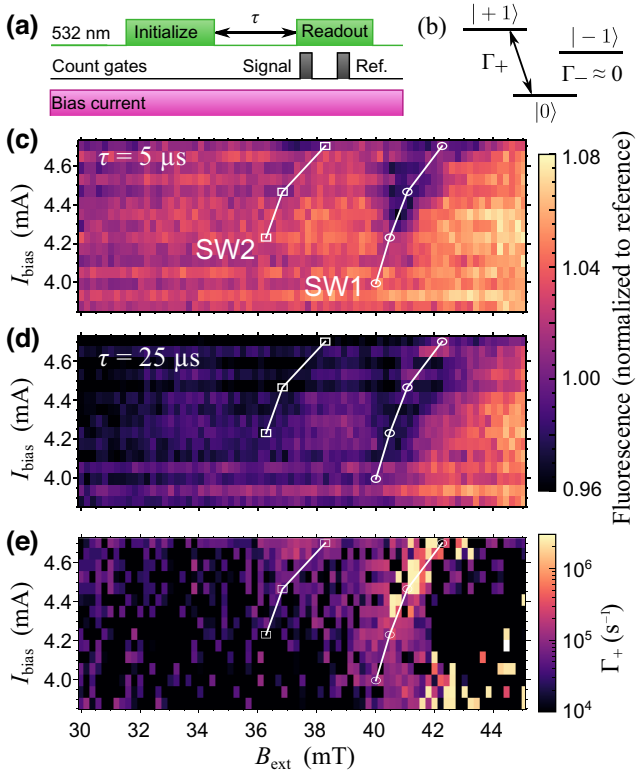

FIG. 4. Relaxation measurements. (a) Diagram of the pulse measurement scheme used for relaxometry, showing the 532-nm laser pulses for initialization and readout, separated by delay τ, with gated photon counting for the "signal" and "reference" times. Bias current is applied throughout. (b) Simplified population rates $\Gamma_\pm$ between the ground ($|0\rangle$) and two excited spin states ($|\pm 1\rangle$). (c),(d) Measured fluorescence during relaxometry for $\tau = 5$ μs and $\tau = 25$ μs, respectively. Fluorescence is normalized by the "reference" counts, and decreases when the magnetic noise from an SW mode is resonant with the N-V. (e) Results of fitting a single-exponential decay model to the fluorescence data for $\tau \in \{5, 10, 15, 20, 25\}$ μs. Open circles (squares) denote the resonance conditions between the N-V and SW1 (SW2) for (c), (d), and (e).

external field and bias are swept. Open circles (squares) show the bias and magnetic field conditions where the probe and spin-wave frequencies are in resonance $\nu_+ = \nu_{SW1}$ ($\nu_+ = \nu_{SW2}$). Immediately apparent are the dips in fluorescence that occur at biases near and above the STO thresholds. [Note that the apparent increase in fluorescence above $I_{bias} = 4.5$ mA in Fig. 4(d) is an artifact of the normalization procedure: when Γ_+ exceeds the polarization rate during the laser pulse, the initialization fidelity is diminished, which reduces the reference counts, increasing the normalized signal.]

Next, we fit time-series data spanning $5 < \tau < 25$ μs at each applied field and bias to a single-exponential decay in order to extract the relaxation rate Γ_+ shown in Fig. 4(e). We note that, while the all-optical relaxometry approach is experimentally simple to implement, parameter extraction from the fluorescence measurements is susceptible to crosstalk from other noise sources, such as spin mixing between 0 and −1 states near the excited-state level anticrossing at $B_{ext} = 50.4$ mT during optical pumping. Furthermore, the restriction of $\tau \in [5, 25]$ μs limits our ability to discern relaxation rates far outside the range 0.04 to 0.2 μs^{-1}. Nevertheless, the simplistic approach to decay fitting is in agreement with our interpretation of the N-V probing two spin-wave modes and confirms the STO threshold at $I_{bias} = 4.3$ mA, above which the measured magnetic-noise-induced relaxation rate increases by orders of magnitude. The measured value $\Gamma_+ > 1$ μs^{-1} when SW1 undergoes auto-oscillation is also consistent with the rates needed to form the features seen in ODMR, since the relaxation rates required to see any features in the latter must be comparable to the spin polarization rate of about 5 MHz from optical pumping.

VI. CONCLUSION

We report N-V ODMR and spin relaxation measurements of a free-running STO, and the ODMR spectral signatures of parametric phase locking, STO frequency pulling and modulation, and the quenching of one STO mode by another SW. The interpretations of all but the last (multi-SW) feature are validated by a simple macrospin simulation. Beyond these demonstrations, pulsed ODMR might enable distinguishing between coherent phase locking and noisy auto-oscillations, and relaxometry protocols can be improved and expedited with MW spin preparation and adaptive pulse pattern generation [52].

To maximize the utility of these testbed-system results, these techniques should be implemented in scanning probe systems, enabling one to resolve the spatial distribution of SW modes below the diffraction limit of laser light. In particular, this would complement and improve upon existing Brillouin light scattering techniques used to determine the localization of mutual synchronization in STO arrays [53]. Even using standard ODMR, we demonstrate a measurement capable of observing STO dynamics far beyond what is possible with device-scale resistive readout.

ACKNOWLEDGMENTS

This work is partially supported by the National Science and Engineering Research Council (NSERC RGPIN 435554-13, RGPIN-2020-04095), Canada Research Chairs (229003 and 231949), Fonds de Recherche—Nature et Technologies (FRQNT PR-181274), the Canada Foundation for Innovation (Innovation Fund 2015 project 33488 and LOF/CRC 229003), and l'Institut Transdisciplinaire d'Information Quantique (INTRIQ). L.C. is a CIFAR fellow in the Quantum Information Science program. A.S. acknowledges support from the NSERC CREATE program QSciTech. M.C.-M. acknowledges financial support from the First Nation Council of Innu Essipit.

A.S. designed the experiment, acquired and analyzed the data, simulated the measurement, led the fabrication of the sample, and cowrote the manuscript. M.C.-M. performed initial characterization of N-V centers in proximity of candidate devices to select for microfabricating connections. B.R. developed the fabrication process for device connections. P.B. developed the subtractive fabrication process for patterning the nanowires. L.C. advised on experiments and simulations, and cowrote the paper. J.S. advised on experiments and simulations, created the magnetic domain solver used for simulations, and cowrote the paper.

APPENDIX A: DEVICE FABRICATION

We use an electronic grade diamond (element6) with a (001) surface as the substrate for the nanofabricated device. The diamond has been implanted with a densely populated layer of N-V centers created via $^{15}N^+$ ion implantation described in our previous experiment [36]. We fabricate the device in this study using a two-step process. To define the nanowires, 5-nm layers of permalloy and platinum are deposited by electron-beam evaporation uniformly over the diamond surface, and a 10-nm-thick alumina mask in the shape of the nanowire is deposited by electron-beam lithography and liftoff. The surrounding metal is then removed with an argon ion mill. We find that this step greatly reduces the N-V spin state fluorescence contrast, but that an oxygen plasma "asher" can recover the spin contrast without damaging the magnetic structures (see Appendix B). Finally, KOH is used to remove the alumina layer, allowing for top electrical contact. We then select devices with well-coupled N-V centers nearby, and optically reimage their positions relative to the nearby alignment marks (compensating for the systematic drift during their initial patterning, e.g., due to charging effects). Without this realignment step, deviations of up to 1 μm

from the design specification preclude reliably creating lead overlaps of 0.3 μm.

APPENDIX B: N-*V* ODMR CONTRAST RECOVERY

Following the argon ion milling step above, we wirebond a stripline above the diamond approximately 100 μm from the devices of interest and use this to generate microwave fields for testing nearby emitters. We noticed that ODMR contrasts from all N-*V* centers were reduced by a factor of about 8 (from 16% to 2%), as shown in Fig. 5, presumably from the ion mill step, consistent with an altered surface chemistry known to decrease the charge stability of the negatively charged N-*V* centers and favor the magnetically insensitive neutral state [54,55]. To repair the damaged surface termination, we expose the patterned diamond surface to an oxygen plasma [56] from a plasma asher (Nanoplas DSB6000, 400-W rf power, 40 sccm O2 flow, 0.4-torr chamber pressure at 45 °C). By wirebonding a stripline across the surface between each plasma exposure and measuring the ODMR contrast, we observe that the contrast measured over 40 emitters (not the same emitters as before the ion etch) recovers the nominal value after about 50 min of exposure. Note that the variation in the observed contrast across the sampled N-*V* centers may be partially due to variation in the local environments, as well as variation in the Rabi frequency, which was not controlled, as each emitter may have a different orientation relative to the microwave magnetic field.

While the plasma asher was shown to repair the measured spin contrast for the near-surface N-*V* centers, we also verified that the processing was compatible with our fabrication flow. Specifically, we conducted AFM measurements of the alumina/Pt/Py trilayer patterned devices after each exposure, as well as after the alumina was removed by a KOH etch, in order to verify that the plasma did not etch the surface or patterned materials. Additionally, the ashing process was shown to not noticeably affect the magnetization of Py (e.g., by oxidization through the side walls) by measuring the splitting of N-*V* spin resonances (partially set by the dipole field of the Py layer) at two locations near the nanowire after each step. At each step of the process, the so-inferred stray field from the Py layer was unchanged from the original value within our approximate 10% measurement uncertainty.

APPENDIX C: SIMULATION PARAMETERS OF ODMR

Following the treatment by Dréau *et al.* [51], we model the N-*V* steady-state spin population under continuous-wave excitation to simulate an analogue of the measured fluorescence. Specifically, we respectively model the steady-state populations p_0 and p_1 of the $m_s = 0$ and $m_s = 1$ states as

$$p_1 = \frac{\Gamma_1[(2\pi)^2(\nu_{\mathrm{MW}} - \nu_1)^2 + \Gamma_2^2] + \Gamma_2\Omega_R^2/2}{(2\Gamma_1 + \Gamma_p)[(2\pi)^2(\nu_{\mathrm{MW}} - \nu_1)^2 + \Gamma_2^2] + \Gamma_2\Omega_R^2}, \tag{C1}$$

$$p_0 = 1 - p_1, \tag{C2}$$

where Ω_R and Γ_1 are the Rabi frequency and relaxation rate defined in the main text; $\Gamma_p = \Gamma_p^\infty s/(1+s)$ is the optically induced polarization rate and $\Gamma_2 = \Gamma_2^* + \Gamma_c^\infty s/(1+s) + \frac{1}{2}\Gamma_1$ is the spin dephasing rate. These in turn depend on the saturation parameter $s = 0.5$ (corresponding to the optical intensity used in these experiments), the optically induced polarization rate at saturation of $\Gamma_p^\infty = 5 \times 10^6\ \mathrm{s}^{-1}$, the optical cycling rate at saturation of $\Gamma_c^\infty = 8 \times 10^7\ \mathrm{s}^{-1}$, and the inhomogeneous dephasing rate $\Gamma_2^* = 2 \times 10^5\ \mathrm{s}^{-1}$.

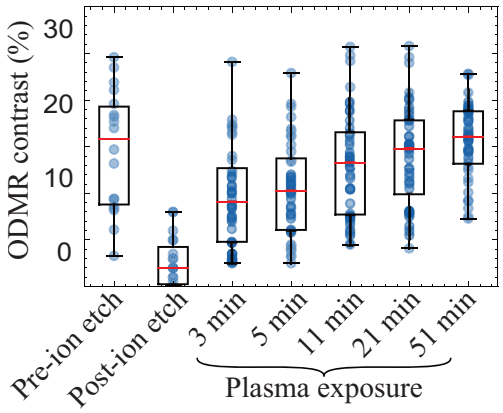

FIG. 5. ODMR contrast damage and recovery. Measured NV-ODMR contrast for each process step. Each dot is a measurement of a fluorescent emitter's ODMR contrast, and the box plot shows the four quadrants in which the data lie.

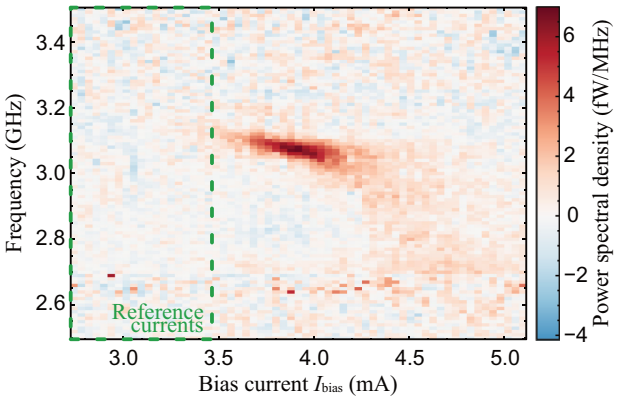

FIG. 6. Power spectral density of a second device. Spectrum analyzer measurement of an STO response from the same chip as the device studied in this paper. The power spectral density is shown relative to the measured values averaged over the reference currents shown in the green dashed box.

As discussed in the main text, we decompose the time-dependent field from the simulated magnetization at the N-V center's position into left- and right-circulating drives, which we note can lead to double counting of the spin-flipping dynamics under some parameter ranges. Specifically, when the STO is phase locked to the parametric drive, the magnet will drive coherent oscillations in the N-V such that $\Omega_R > 0$, but if the drive frequency is exactly resonant with the N-V center's harmonic as $\nu_{MW} = 2\nu_1$ then the Fourier transform definition for $\Gamma_1 > 0$ also plays a role in mixing the spin. Because this double counting only occurs for values of $|\nu_{MW} - 2\nu_1| < \Delta\nu_{FFT}$ (where $\Delta\nu_{FFT} = 5$ MHz is the resolution of the Fourier transform), we neglect it, as it does not qualitatively change the results.

APPENDIX D: TRANSPORT VERIFICATION OF THE STO

To confirm that the fabrication process leads to coherent, free-running STOs with signals detectable by conventional means, we use a spectrum analyzer having a resolution bandwidth of 22 MHz to measure the power spectral density of microwave electrical currents induced by the mixture of oscillating magnetoresistance with the bias currents [13]. Although the device studied in this article was destroyed before we could perform this test, we measured the electrical spectrum in a device from the same chip and fabrication run with lateral dimensions of $6 \times 0.3\ \mu m^2$, as shown in Fig. 6. As the bias current is increased above the STO threshold of about 3.6 mA, a spectral line with a < 50-MHz linewidth appears and decreases in frequency with bias, consistent with the macrospin model. This measurement further validates that the features in the N-V fluorescence data can be attributed to the auto-oscillations of an STO.

[1] V. V. Kruglyak, S. O. Demokritov, and D. Grundler, Magnonics, J. Phys. D: Appl. Phys. **43**, 264001 (2010).

[2] A. V. Chumak, A. A. Serga, and B. Hillebrands, Magnon transistor for all-magnon data processing, Nat. Commun. **5**, 1 (2014).

[3] A. V. Chumak, V. I. Vasyuchka, A. A. Serga, and B. Hillebrands, Magnon spintronics, Nat. Phys. **11**, 453 (2015).

[4] Q. Wang, M. Kewenig, M. Schneider, R. Verba, F. Kohl, B. Heinz, M. Geilen, M. Mohseni, B. Lägel, F. Ciubotaru, C. Adelmann, C. Dubs, S. D. Cotofana, O. V. Dobrovolskiy, T. Brächer, P. Pirro, and A. V. Chumak, A magnonic directional coupler for integrated magnonic half-adders, Nat. Electron. **3**, 765 (2020).

[5] S. Lequeux, J. Sampaio, V. Cros, K. Yakushiji, A. Fukushima, R. Matsumoto, H. Kubota, S. Yuasa, and J. Grollier, A magnetic synapse: Multilevel spin-torque memristor with perpendicular anisotropy, Sci. Rep. **6**, 1 (2016).

[6] M. Romera, P. Talatchian, S. Tsunegi, F. Abreu Araujo, V. Cros, P. Bortolotti, J. Trastoy, K. Yakushiji, A. Fukushima, H. Kubota, S. Yuasa, M. Ernoult, D. Vodenicarevic, T. Hirtzlin, N. Locatelli, D. Querlioz, and J. Grollier, Vowel recognition with four coupled spin-torque nano-oscillators, Nature **563**, 230 (2018).

[7] T. Shibata, T. Shinohara, T. Ashida, M. Ohta, K. Ito, S. Yamada, Y. Terasaki, and T. Sasaki, Linear and symmetric conductance response of magnetic domain wall type spin-memristor for analog neuromorphic computing, Appl. Phys. Express **13**, 043004 (2020).

[8] S. A. Siddiqui, S. Dutta, A. Tang, L. Liu, C. A. Ross, and M. A. Baldo, Magnetic domain wall based synaptic and activation function generator for neuromorphic accelerators, Nano Lett. **20**, 1033 (2020).

[9] J. Grollier, D. Querlioz, K. Y. Camsari, K. Everschor-Sitte, S. Fukami, and M. D. Stiles, Neuromorphic spintronics, Nat. Electron. **3**, 360 (2020).

[10] S. Yang, J. Shin, T. Kim, K.-W. Moon, J. Kim, G. Jang, D. S. Hyeon, J. Yang, C. Hwang, Y. Jeong, and J. P. Hong, Integrated neuromorphic computing networks by artificial spin synapses and spin neurons, NPG Asia Mater. **13**, 1 (2021).

[11] C. D. Schuman, S. R. Kulkarni, M. Parsa, J. P. Mitchell, P. Date, and B. Kay, Opportunities for neuromorphic computing algorithms and applications, Nat. Comput. Sci. **2**, 10 (2022).

[12] M. Zahedinejad, H. Fulara, R. Khymyn, A. Houshang, M. Dvornik, S. Fukami, S. Kanai, H. Ohno, and J. Åkerman, Memristive control of mutual spin Hall nano-oscillator synchronization for neuromorphic computing, Nat. Mater. **21**, 81 (2022).

[13] S. I. Kiselev, J. C. Sankey, I. N. Krivorotov, N. C. Emley, R. J. Schoelkopf, R. A. Buhrman, and D. C. Ralph, Microwave oscillations of a nanomagnet driven by a spin-polarized current, Nature **425**, 380 (2003).

[14] W. H. Rippard, M. R. Pufall, S. Kaka, S. E. Russek, and T. J. Silva, Direct-current induced dynamics in $Co_{90}Fe_{10}/Ni_{80}Fe_{20}$ point contacts, Phys. Rev. Lett. **92**, 027201 (2004).

[15] W. H. Rippard, M. R. Pufall, S. Kaka, T. J. Silva, S. E. Russek, and J. A. Katine, Injection locking and phase control of spin transfer nano-oscillators, Phys. Rev. Lett. **95**, 067203 (2005).

[16] A. A. Tulapurkar, Y. Suzuki, A. Fukushima, H. Kubota, H. Maehara, K. Tsunekawa, D. D. Djayaprawira, N. Watanabe, and S. Yuasa, Spin-torque diode effect in magnetic tunnel junctions, Nature **438**, 339 (2005).

[17] J. C. Sankey, P. M. Braganca, A. G. F. Garcia, I. N. Krivorotov, R. A. Buhrman, and D. C. Ralph, Spin-transfer-driven ferromagnetic resonance of individual nanomagnets, Phys. Rev. Lett. **96**, 227601 (2006).

[18] L. Liu, T. Moriyama, D. C. Ralph, and R. A. Buhrman, Spin-torque ferromagnetic resonance induced by the spin Hall effect, Phys. Rev. Lett. **106**, 036601 (2011).

[19] Z. Duan, A. Smith, L. Yang, B. Youngblood, J. Lindner, V. E. Demidov, S. O. Demokritov, and I. N. Krivorotov, Nanowire spin torque oscillator driven by spin orbit torques, Nat. Commun. **5**, 1 (2014).

[20] S. O. Demokritov, B. Hillebrands, and A. N. Slavin, Brillouin light scattering studies of confined spin waves: Linear and nonlinear confinement, Phys. Rep. **348**, 441 (2001).

[21] S. O. Demokritov and V. E. Demidov, Micro-Brillouin light scattering spectroscopy of magnetic nanostructures, IEEE Trans. Magn. **44**, 6 (2007).
[22] A. A. Serga, A. V. Chumak, and B. Hillebrands, YIG magnonics, J. Phys. D: Appl. Phys. **43**, 264002 (2010).
[23] L. J. P. Ament, M. van Veenendaal, T. P. Devereaux, J. P. Hill, and J. van den Brink, Resonant inelastic X-ray scattering studies of elementary excitations, Rev. Mod. Phys. **83**, 705 (2011).
[24] N. Träger, F. Groß, J. Förster, K. Baumgaertl, H. Stoll, M. Weigand, G. Schütz, D. Grundler, and J. Gräfe, Single shot acquisition of spatially resolved spin wave dispersion relations using X-ray microscopy, Sci. Rep. **10**, 1 (2020).
[25] Y. Au, T. Davison, E. Ahmad, P. S. Keatley, R. J. Hicken, and V. V. Kruglyak, Excitation of propagating spin waves with global uniform microwave fields, Appl. Phys. Lett. **98**, 122506 (2011).
[26] H. G. Bauer, J.-Y. Chauleau, G. Woltersdorf, and C. H. Back, Coupling of spinwave modes in wire structures, Appl. Phys. Lett. **104**, 102404 (2014).
[27] L. Rondin, J.-P. Tetienne, S. Rohart, A. Thiaville, T. Hingant, P. Spinicelli, J.-F. Roch, and V. Jacques, Stray-field imaging of magnetic vortices with a single diamond spin, Nat. Commun. **4**, 1 (2013).
[28] M. S. Wolf, R. Badea, and J. Berezovsky, Fast nanoscale addressability of nitrogen-vacancy spins via coupling to a dynamic ferromagnetic vortex, Nat. Commun. **7**, 1 (2016).
[29] P. J. Scheidegger, S. Diesch, M. L. Palm, and C. L. Degen, Scanning nitrogen-vacancy magnetometry down to 350 mK, Appl. Phys. Lett. **120**, 224001 (2022).
[30] J.-P. Tetienne, T. Hingant, L. J. Martínez, S. Rohart, A. Thiaville, L. H. Diez, K. Garcia, J.-P. Adam, J.-V. Kim, J.-F. Roch, I. M. Miron, G. Gaudin, L. Vila, B. Ocker, D. Ravelosona, and V. Jacques, The nature of domain walls in ultrathin ferromagnets revealed by scanning nanomagnetometry, Nat. Commun. **6**, 1 (2015).
[31] H. Zhang, M. J. H. Ku, F. Casola, C. H. R. Du, T. van der Sar, M. C. Onbasli, C. A. Ross, Y. Tserkovnyak, A. Yacoby, and R. L. Walsworth, Spin-torque oscillation in a magnetic insulator probed by a single-spin sensor, Phys. Rev. B **102**, 024404 (2020).
[32] G. Q. Yan, S. Li, T. Yamamoto, M. Huang, N. J. Mclaughlin, T. Nozaki, H. Wang, S. Yuasa, and C. R. Du, Electric-field-induced coherent control of nitrogen-vacancy centers, Phys. Rev. Appl. **18**, 064031 (2022).
[33] I. Bertelli, J. J. Carmiggelt, T. Yu, B. G. Simon, C. C. Pothoven, G. E. W. Bauer, Y. M. Blanter, J. Aarts, and T. van der Sar, Magnetic resonance imaging of spin-wave transport and interference in a magnetic insulator, Sci. Adv. **6**, eabd3556 (2020).
[34] B. G. Simon, S. Kurdi, J. J. Carmiggelt, M. Borst, A. J. Katan, and T. van der Sar, Filtering and imaging of frequency-degenerate spin waves using nanopositioning of a single-spin sensor, Nano Lett. **22**, 9198 (2022).
[35] C. Gonzalez-Ballestero, T. van der Sar, and O. Romero-Isart, Towards a quantum interface between spin waves and paramagnetic spin baths, Phys. Rev. B **105**, 075410 (2022).
[36] A. Solyom, Z. Flansberry, M. A. Tschudin, N. Leitao, M. Pioro-Ladrière, J. C. Sankey, and L. I. Childress, Probing a spin transfer controlled magnetic nanowire with a single nitrogen-vacancy spin in bulk diamond, Nano Lett. **18**, 6494 (2018).
[37] E. Lee-Wong, R. Xue, F. Ye, A. Kreisel, T. van der Sar, A. Yacoby, and C. R. Du, Nanoscale detection of magnon excitations with variable wavevectors through a quantum spin sensor, Nano Lett. **20**, 3284 (2020).
[38] H. Suhl, The theory of ferromagnetic resonance at high signal powers, J. Phys. Chem. Solids **1**, 209 (1957).
[39] Z. Haghshenasfard, H. T. Nguyen, and M. G. Cottam, Suhl instabilities for spin waves in ferromagnetic nanostripes and ultrathin films, J. Magn. Magn. Mater. **426**, 380 (2017).
[40] C. L. Degen, Scanning magnetic field microscope with a diamond single-spin sensor, Appl. Phys. Lett. **92**, 243111 (2008).
[41] P. Maletinsky, S. Hong, M. S. Grinolds, B. Hausmann, M. D. Lukin, R. L. Walsworth, M. Loncar, and A. Yacoby, A robust scanning diamond sensor for nanoscale imaging with single nitrogen-vacancy centres, Nat. Nanotechnol. **7**, 320 (2012).
[42] B. G. Simon, S. Kurdi, H. La, I. Bertelli, J. J. Carmiggelt, M. Ruf, N. de Jong, H. van den Berg, A. J. Katan, and T. van der Sar, Directional excitation of a high-density magnon gas using coherently driven spin waves, Nano Lett. **21**, 8213 (2021).
[43] T. X. Zhou, J. J. Carmiggelt, L. M. Gächter, I. Esterlis, D. Sels, R. J. Stöhr, C. Du, D. Fernandez, J. F. Rodriguez-Nieva, F. Büttner, E. Demler, and A. Yacoby, A magnon scattering platform, Proc. Natl. Acad. Sci. U.S.A. **118**, e2019473118 (2021).
[44] J.-P. Tetienne, L. Rondin, P. Spinicelli, M. Chipaux, T. Debuisschert, J.-F. Roch, and V. Jacques, Magnetic-field-dependent photodynamics of single NV defects in diamond: An application to qualitative all-optical magnetic imaging, New J. Phys. **14**, 103033 (2012).
[45] P. Dürrenfeld, E. Iacocca, J. Åkerman, and P. K. Muduli, Parametric excitation in a magnetic tunnel junction-based spin torque oscillator, Appl. Phys. Lett. **104**, 052410 (2014).
[46] J. C. Sankey, I. N. Krivorotov, S. I. Kiselev, P. M. Braganca, N. C. Emley, R. A. Buhrman, and D. C. Ralph, Mechanisms limiting the coherence time of spontaneous magnetic oscillations driven by dc spin-polarized currents, Phys. Rev. B **72**, 224427 (2005).
[47] J. P. Nibarger, R. Lopusnik, Z. Celinski, and T. J. Silva, Variation of magnetization and the Landé g factor with thickness in Ni–Fe films, Appl. Phys. Lett. **83**, 93 (2003).
[48] Z. Duan, C. T. Boone, X. Cheng, I. N. Krivorotov, N. Reckers, S. Stienen, M. Farle, and J. Lindner, Spin-wave modes in permalloy/platinum wires and tuning of the mode damping by spin Hall current, Phys. Rev. B **90**, 024427 (2014).
[49] J. A. Osborn, Demagnetizing factors of the general ellipsoid, Phys. Rev. **67**, 351 (1945).
[50] W. F. Brown, Thermal fluctuations of a single-domain particle, Phys. Rev. **130**, 1677 (1963).
[51] A. Dréau, M. Lesik, L. Rondin, P. Spinicelli, O. Arcizet, J.-F. Roch, and V. Jacques, Avoiding power broadening in optically detected magnetic resonance of single NV defects for enhanced dc magnetic field sensitivity, Phys. Rev. B **84**, 195204 (2011).

[52] M. Caouette-Mansour, A. Solyom, B. Ruffolo, R. D. McMichael, J. Sankey, and L. Childress, Robust spin relaxometry with fast adaptive Bayesian estimation, Phys. Rev. Appl. **17**, 064031 (2022).

[53] M. Zahedinejad, A. A. Awad, S. Muralidhar, R. Khymyn, H. Fulara, H. Mazraati, M. Dvornik, and J. Åkerman, Two-dimensional mutually synchronized spin Hall nano-oscillator arrays for neuromorphic computing, Nat. Nanotechnol. **15**, 47 (2020).

[54] V. Petráková, A. Taylor, I. Kratochvílová, F. Fendrych, J. Vacík, J. Kučka, J. Štursa, P. Cígler, M. Ledvina, A. FiŠerová, P. Kneppo, and M. Nesládek, Luminescence of nanodiamond driven by atomic functionalization: Towards novel detection principles, Adv. Funct. Mater. **22**, 812 (2012).

[55] K.-M. C. Fu, C. Santori, P. E. Barclay, and R. G. Beausoleil, Conversion of neutral nitrogen-vacancy centers to negatively charged nitrogen-vacancy centers through selective oxidation, Appl. Phys. Lett. **96**, 121907 (2010).

[56] F. Fávaro de Oliveira, S. A. Momenzadeh, Y. Wang, M. Konuma, M. Markham, A. M. Edmonds, A. Denisenko, and J. Wrachtrup, Effect of low-damage inductively coupled plasma on shallow nitrogen-vacancy centers in diamond, Appl. Phys. Lett. **107**, 073107 (2015).